Electronic supplementary information

Rational construction of porous marigold flower-like nickel molybdenum phosphates via ion exchange for high-performance long-lasting hybrid supercapacitors

Ampasala Surya Kiran, Bhimanaboina Ramulu, Shaik Junied Arbaz, Edugulla Girija Shankar, Manchi Nagaraju, and Jae Su Yu*

Department of Electronics and Information Convergence Engineering, Kyung Hee University, 1732 Deogyeong-aero, Gihung-gu, Yongin-si, Gyeonggi-do 17104, Republic of Korea

*Address correspondence to jsyu@khu.ac.kr

Section I: Chemicals and materials

The following chemicals and materials were utilized in this experiment. Analytical grade chemicals including nickel nitrate hexahydrate ($Ni(NO_3)_2 \cdot 6H_2O$), sodium molybdate dihydrate ($H_4MoNa_2O_6$), sodium hypophosphate monohydrate (H_2NaO_3P), urea (CH_4N_2O), N-methyl-2-pyrrolidone (NMP, C_5H_9NO), super-P carbon black, activated carbon (AC) powder, and polyvinylidene difluoride (PVDF, $-(C_2H_2F_2)n-$) were purchased from Sigma Aldrich Co. Potassium hydroxide (KOH), ethanol (C_2H_5OH) (95%), and hydrochloric acid (HCl) were purchased from Daejung Chemicals. Lab-made de-ionized water (DIW) was utilized as the solvent.

Section II: Characterization techniques

A field-emission scanning electron microscope (FE-SEM, Carl Zeiss, LEO SUPRA 55, 5 kV) was used to study the synthesized morphology of the prepared samples. A transmission electron microscope (TEM, JEM 200CX, JEOL, 200 kV) was used to identify the intrinsic structural properties of the samples. The elements in the synthesized samples and the elemental distribution on the obtained morphology were examined by energy-dispersive X-ray (EDX) spectroscopy and elemental mapping analyses, respectively, equipped to the FE-SEM. The crystalline phase of the synthesized sample was inspected by the X-ray diffraction (XRD, Cu Kα radiation, M18XHF-SRA, Mac Science) technique. The surface chemical composition of the elements in the sample were detected by X-ray photoelectron spectroscopy (XPS, Thermo Electron MultiLab2000) and Inductively coupled plasma (ICP, Direct Reading Echelle ICP, LEEMAN) spectrscopy measurements. Brunauer-Emmett-Teller (BET) and Barrett-Joyner-Halenda (BJH) analyses (BELSORP-max00131) were performed on the prepared materials to estimate their surface area and pore size, respectively. Fourier-transform infrared

(FTIR, Spectrum One System Perkin-Elmer) spectroscopy was used to determine the functional groups presented in the prepared materials.

Section III: Electrochemical measurements and necessary equations

The electrochemical properties of individual electrode materials were analyzed via cyclic voltammetry (CV), galvanostatic charge-discharge (GCD), and electrochemical impedance spectroscopy (EIS) measurements in a typical three-electrode configuration in 2 M KOH electrolyte using IviumStat electrochemical workstation (IviumStat Technologies). To prepare the working electrode, initially, nickel foam (NF) stripes were cut (1×2 cm^2), cleaned with 1 M HCl and subsequently with acetone, and dried in an oven of 80 °C for 30 min to remove any traces of the oxide layer. Next, a homogenous slurry was prepared by grinding the UNMP NPs@MSs, PVDF, and super-P carbon black electrode materials in a weight ratio of 80:10:10, respectively, followed by a few drops of NMP. The obtained slurry was brushed coated on NF in a 1×1 cm^2 area and dried at 80 °C for 6 h. Approximately 2 mg cm^{-2} active material was coated for all the prepared electrodes. A similar procedure was followed to prepare the working electrode of the remaining electrode materials. Afterwards, for electrochemical analysis in a three-electrode set-up, the prepared electrodes (individually), Ag/AgCl, and platinum (Pt) wire were employed as working, reference, and counter electrodes, respectively.

The areal capacity values in a three-electrode scheme as well as the areal capacitance and areal energy/power density values in a two-electrode scheme were calculated using the below equations: [S1,S2]

$$C_A = \frac{2I \times \int V(t)dt}{a \times \Delta V} \tag{S1}$$

$$C = \frac{I \times \Delta t}{a \times \Delta V} \tag{S2}$$

$$E = \frac{I \times \int V(t)dt}{a} \qquad\qquad (S3)$$

$$P = \frac{E}{\Delta t} \qquad\qquad (S4)$$

where 'C_A' is the areal capacity (Ah cm^{-2}), 'I' is the applied current (A), 'Δt' is the discharge time (s), 'C' is the areal capacitance (F cm^{-2}), '$\int V(t)dt$' is the integral area, 'ΔV' is the potential window (V), 'E' is the areal energy density (Wh cm^{-2}), and 'P' is the areal power density (W cm^{-2}).
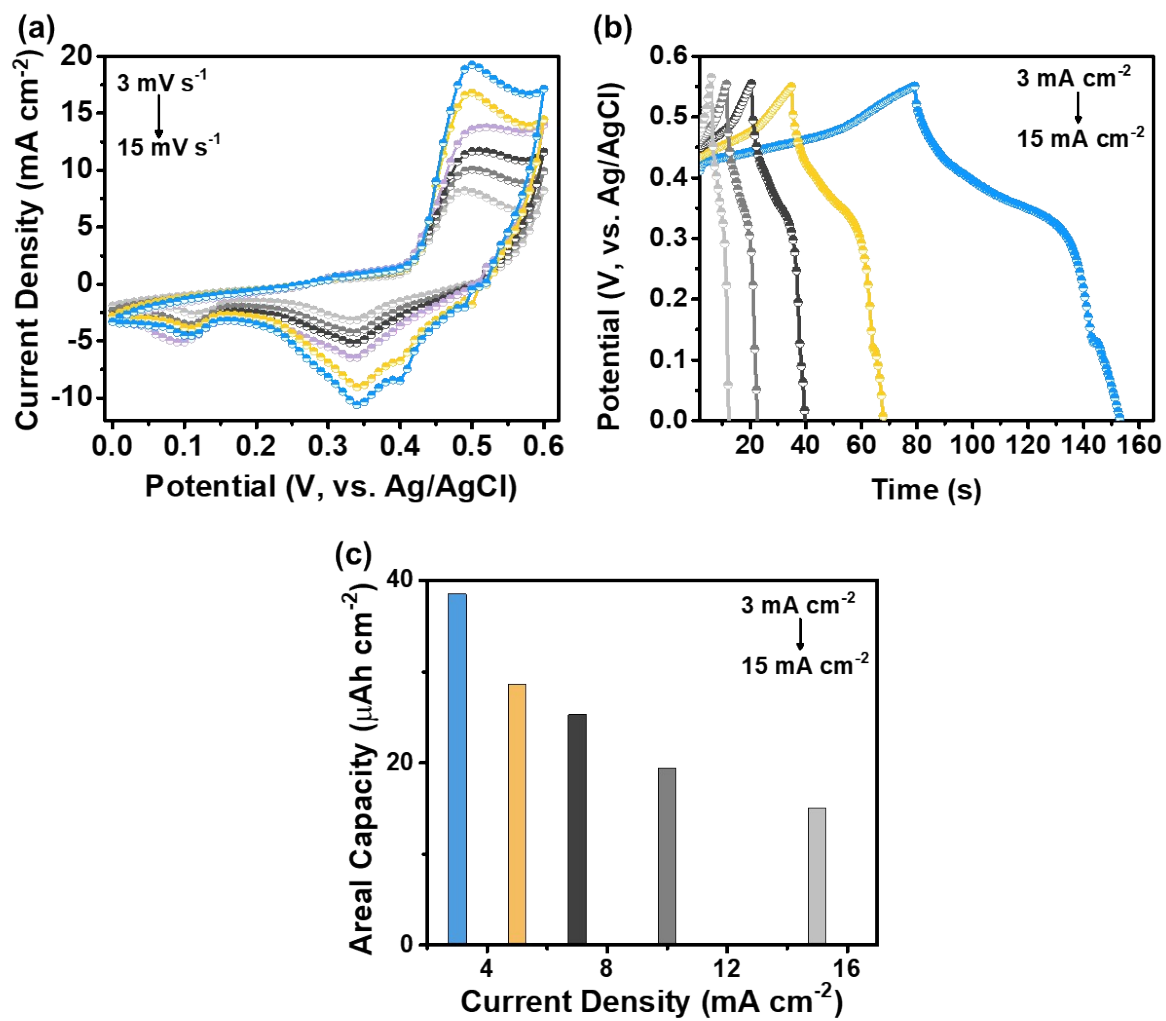
Section IV: Electrochemical properties of NMP/NF and NM/NF electrodes

The electrochemical characteristics of the NMP/NF electrode are given in Fig. S1. Fig. S1(a) shows the CV curves measured under the fixed potential window of 0-0.6 V at different scan rates ranging from 3 to 15 mV s^{-1}. Every curve consists of a single high-intensity oxidation peak and two low-intensity reduction peaks. This signifies that the different transition metals present in the sample undergo reduction at different potentials. Meanwhile, their corresponding oxidation peak was merged into a single high-intensity peak, thereby indicating imbalanced redox reactions. However, the shape and size of the CV curves increased with increasing the scan rate, proving that the current response is proportional to the scan rate. Fig. S1(b) shows the GCD curves of the same electrode. These curves are non-linear, indicating the battery-type behavior of the material. However, due to the lack of proper morphology, the electrode displayed low discharge time even at the initial current density of 3 mA cm^{-2}. Based on this GCD profile, the areal capacity values were calculated in Fig. S1(b). The NMP/NF electrode showed an areal capacity value of 61.2 µAh cm^{-2} at the initial current density of 3 mA cm^{-2} and a high current density of 15 mA cm^{-2}, it exhibited a value of 21.8 µAh cm^{-2}.

The electrochemical properties of the NM/NF electrode are given in Fig. S2. The CV curves were analyzed within the potential window of 0-0.6 V at scan rates ranging from 3 to 15 mV s^{-1}. The CV curves contain broad oxidation and reduction peaks, signifying the merged redox properties of both Ni and Mo. The appearance of redox peaks at every scan rate indicates good redox reversibility. Moreover, the CV response is in proportion to the scan rate. The GCD curves in Fig. S2(b) contain nonlinear discharge curves, emphasizing its battery-type behavior. The lowest discharge time at a current density of 3 mA cm^{-2} evidences that the material could not achieve high performance due to the absence of a phosphorous source. Furthermore, due to the absence of a decent morphology, the nanoparticles could not obtain a high surface area and hence failed to accommodate a large number of charges during the electrochemical activity. Fig. S2(c) shows the areal capacity values based on the respective GCD profile of the NM/NF electrode. Here, it is seen that the electrode delivered a maximum areal capacity value of 38.2 μAh cm^{-2} at an initial current density of 3 mA cm^{-2}.
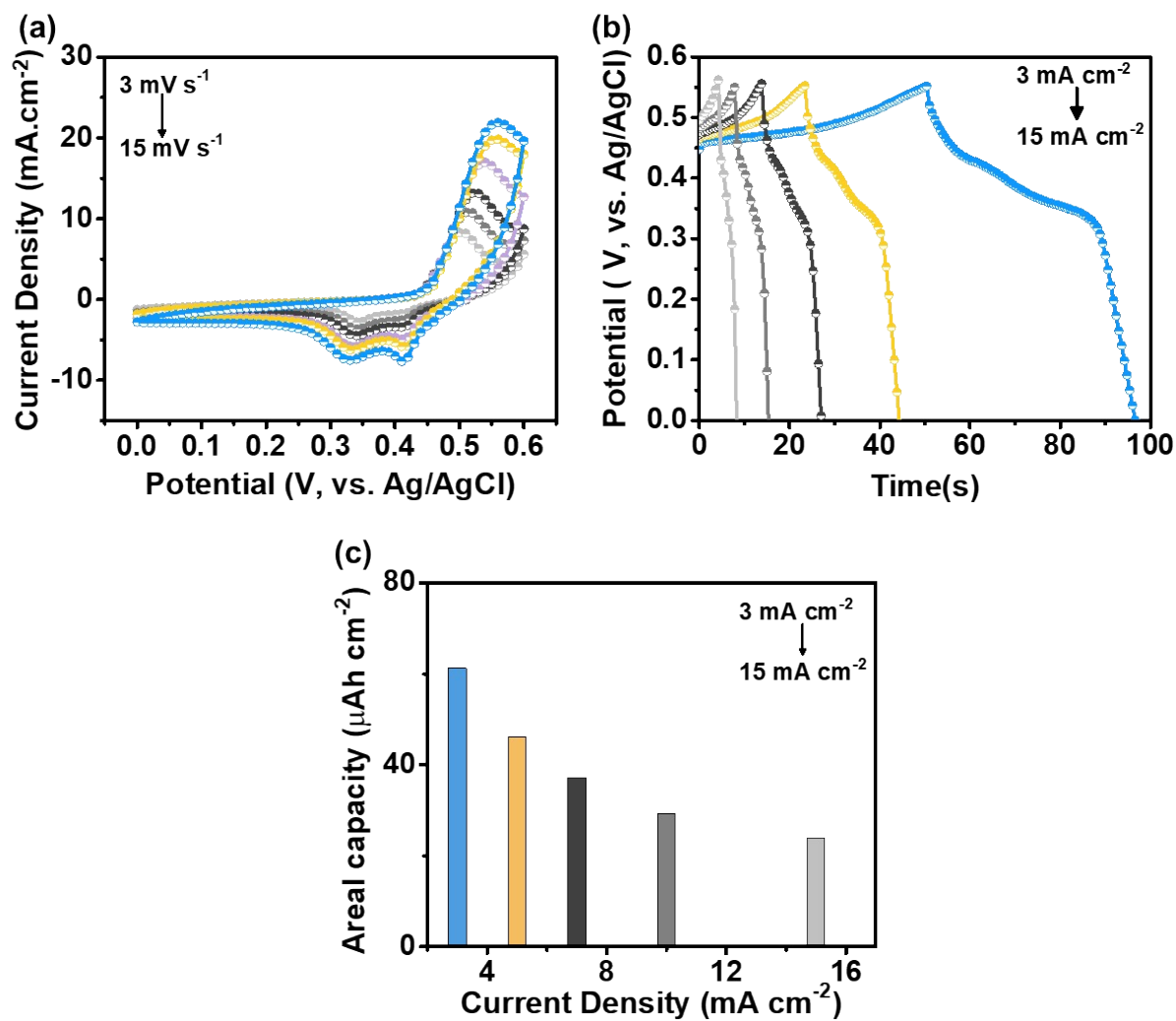
Fig. S1. Electrochemical properties of the NMP/NF electrode. (a) CV curves at various scan rates. (b) GCD curves at various current densities. (c) Areal capacity values at various current densities.

Fig. S2. Electrochemical properties of the NM/NF electrode. (a) CV curves at various scan rates. (b) GCD curves at various current densities. (c) Areal capacity values at various current densities.
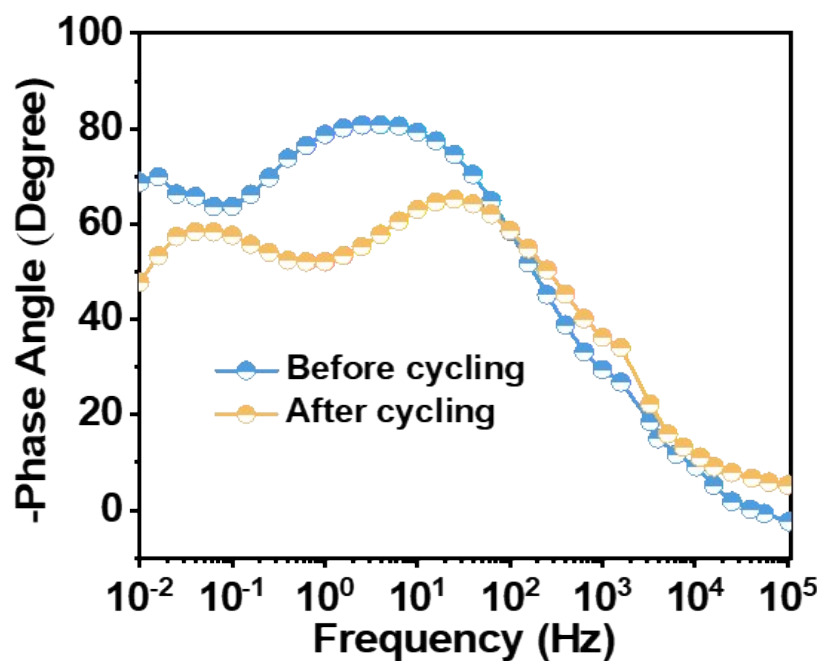
Fig. S3. Bode plots of the prepared UNMP NPs@MSs electrode before and after the cycling test.

Table S1. Comparison of capacitance/capacity performance of the UNMP NPs@MSs electrode with previously published electrode materials.

Active material	Preparation method	Electrolyte	Number of cycles/ Retention (%)	Test condition	Areal capacity	Ref.
Bi_2S_3@g-C_3N_4	Hydrothermal	1M KOH	7500 / 83.84%	1 mA/cm^2	41.53 μAh cm^{-2}	[S3]
$MnCo_2O_{4.5}$@ δ-MnO_2	Wet-chemical synthesis	1M Na_2SO_4	1000 / 90%	1 mA/cm^2	9.73 μAh cm^{-2}	[S4]
Hybrid $NiMoO_4$/rGO	Hydrothermal	2M KOH	3000 / 66.1%	0.8 mA/cm^2	133.5 μAh cm^{-2}	[S5]
Co_3O_4@$NiCo_2O_4$	Hydrothermal	1M KOH	5000 / 100.7%	3 mA/cm^2	147 μAh cm^{-2}	[S6]
CNTs@CeO_2 HTs	Biomorphic method	1M KOH	2000 / 86.1%	1 mA/cm^2	70.7 μAh cm^{-2}	[S7]
VS_x/Graphite	Simple synthesis	1M KCL	-	0.5 mA/cm^2	34 μAh cm^{-2}	[S8]
$NiCo_2O_4$	Solvothermal	1 M KOH	4000 / 97.6%	2 mA/cm^2	152.7 μAh cm^{-2}	[S9]
UNMP	**Ion exchange**	**2 M KOH**	**50000 / 99.5%**	**3 mA/cm^2**	**166.6 μAh cm^{-2}**	**This Work**

**Section V: Preparation of negative electrode (AC/NF)**

To fabricate the negative electrode, the activated carbon (AC) was utilized as the active material owing to its high porosity. These pores increase the specific surface area of carbon particles and play a key role during a charge storage operation, through non-faradic reactions. The AC powder, PVDF, and super-P black were considered in the weight ratios of 80:10:10 and were finely ground by adding a few drops of NMP to obtain a smooth slurry. The slurry was brush-coated onto the cleaned NF of an active area 1×1 cm^{-2} and dried in an oven at 80 ^{o}C for 24 h. The dried electrode was later pressed under a pressure of 10 MPa to obtain the AC/NF.

Section VI: Electrochemical properties of the negative electrode (AC/NF)

The electrochemical properties of the AC/NF electrode were measured in a three-electrode system in a 2 M KOH aqueous electrolyte solution. Fig. S3 shows the CV curves of the AC/NF electrode measured at different scan rates of 10-100 mV s^{-1} within the potential range of -1 to 0 V. All the CV curves were in quasi-rectangular shape, evidencing the non-faradic charge storage mechanism. The shape of the CV curves was in proportion to the scan rate. Fig. S3(b) shows the GCD curves of the AC/NF electrode at current densities ranging from 3-15 mA cm^{-2} under the potential window of -1 to 0 V. The linearity within the curves indicates the adsorption and desorption processes taking place during the charging and discharging cycles. By using these discharge curves, at an initial current density of 3 mA cm^{-2}, the AC/NF electrode exhibited an areal capacitance of 143.2 μAh cm^{-2}.
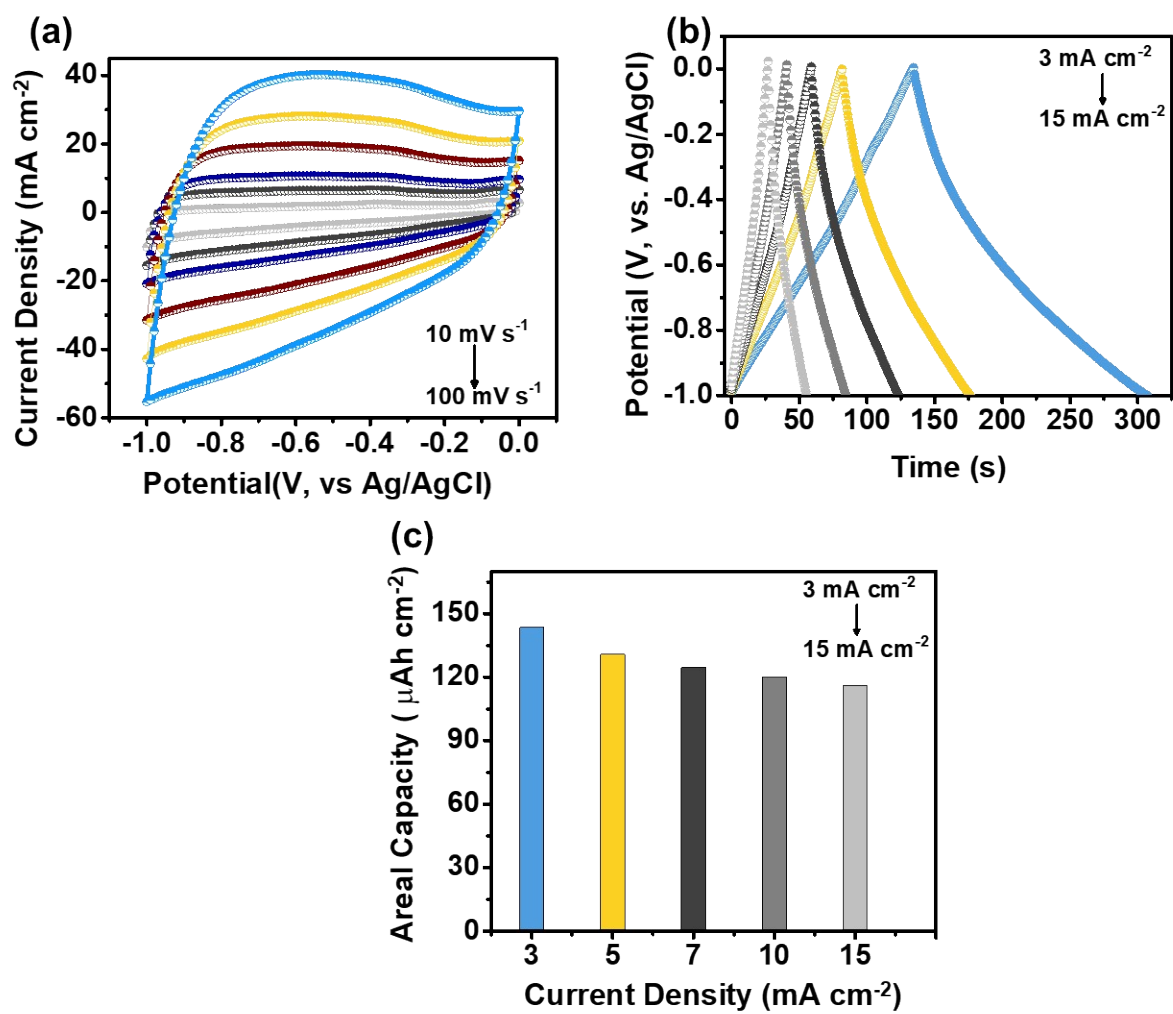
Fig. S4. (a) CV and (b) GCD curves of the AC/NF electrode measured at various scan rates and current densities, respectively. (c) Areal capacity values of the AC/NF electrode.
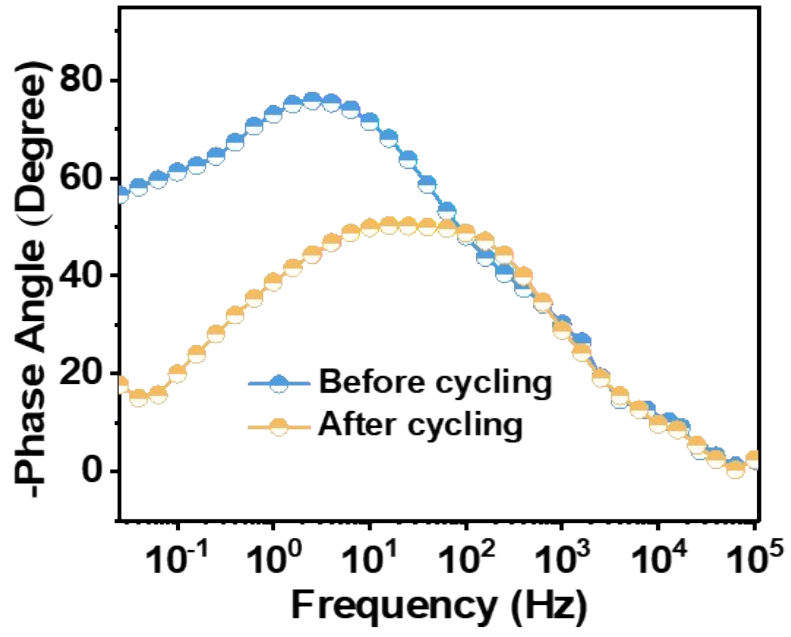
Fig. S5. Bode plots of the HSC device before and after the cycling test.

Table S2. Energy and power density values compared to the previously reported works.

Positive electrode	Negative electrode	Energy density	Power density	Ref.
NiMo-HCNF	Activated carbon (AC)	30 Wh kg^{-1}	403 W kg^{-1}	[S10]
β-NiMoO$_4$-CoMoO$_4$·xH$_2$O	Activated carbon (AC)	28 W h kg^{-1}	100 W kg^{-1}	[S11]
Nickel cobalt oxide@nickel molybdenum oxide	Activated carbon (AC)	11.9 Wh kg^{-1}	800 W kg^{-1}	[S12]
NiCo$_2$S$_4$-C-MoS$_2$	Activated carbon (AC)	27.7 Wh kg^{-1}	400 W kg^{-1}	[S13]
CoMoO$_4$@3D graphene	Activated carbon (AC)	21.1 Wh kg^{-1}	300 W kg^{-1}	[S14]
NiMoO$_4$·xH$_2$O	Activated carbon (AC)	34.4 W h kg^{-1}	165 W kg^{-1}	[S15]
UNMP NPs@MSs	**Activated carbon (AC)**	**34.34 Wh kg^{-1}**	**5106.38 W kg^{-1}**	**Our work**

References

[S1]   M. Nagaraju, S.C. Sekhar, S.J. Arbaz, J.S. Yu, Solvothermal-derived nanoscale spinel bimetallic oxide particles rationally bridged with conductive vapor-grown carbon fibers for hybrid supercapacitors. Appl. Surf. Sci. 2021, **563,** 150223.

[S2]   G.S.R. Raju, E. Pavitra, G. Nagaraju, S.C. Sekhar, S.M. Ghoreishian, C.H. Kwak, J.S. Yu, Y.S. Huh, Y.-K. Han, Rational design of forest-like nickel sulfide hierarchical architectures with ultrahigh areal capacity as a binder-free cathode material for hybrid supercapacitors. J. Mater. Chem. A 2018, **6,** 13178-13190.

[S3]   M. Karuppaiah, X. Benadict Joseph, S.-F. Wang, B. Sriram, G. Antilen Jacob, G. Ravi, Engineering architecture of 3D-urchin-like structure and 2d-nanosheets of $Bi_2S_3@$ g-C_3N_4 as the electrode material for a solid-state symmetric supercapacitor. Energy Fuels 2021, **35,** 12569-12580.

[S4]   Y. Li, J. Jian, Y. Fan, H. Wang, L. Yu, G. Cheng, J. Zhou, M. Sun, Facile one-pot synthesis of a $NiMoO_4$/reduced graphene oxide composite as a pseudocapacitor with superior performance. RSC Adv. 2016, **6,** 69627-69633.

[S5]   K. Xu, X. Yang, J. Yang, J. Hu, Synthesis of hierarchical $Co_3O_4@$ $NiCo_2O_4$ core-shell nanosheets as electrode materials for supercapacitor application. J. Alloys Compd. 2017, **700,** 247-251.

[S6]   B. Ramulu, G. Nagaraju, S.C. Sekhar, J.S. Yu, Highly porous CNTs knotted cerium oxide hollow tubes with exalted energy storage performance for hybrid supercapacitors. J. Alloys Compd. 2020, **819,** 152942.

[S7]   S. Ng, K. Ghosh, J. Vyskocil, M. Pumera, Two-dimensional vanadium sulfide flexible graphite/polymer films for near-infrared photoelectrocatalysis and electrochemical energy storage. Chem. Eng. J. 2022, **435,** 135131.

[S8]   S.J. Arbaz, S.C. Sekhar, B. Ramulu, J.S. Yu, Binder-free preparation of bimetallic oxide vertical nanosheet arrays toward high-rate performance and energy density supercapacitors. Int. J. Energy Res. 2021, **45,** 13999-14009.

[S9]   W. He, C. Wang, F. Zhuge, X. Deng, X. Xu, T. Zhai, Flexible and high energy density asymmetrical supercapacitors based on core/shell conducting polymer nanowires/manganese dioxide nanoflakes. Nano Energy 2017, **35,** 242-250.

[S10] V. S. Budhiraju, R. Kumar, A. Sharma and S. Sivakumar, Structurally stable hollow mesoporous graphitized carbon nanofibers embedded with $NiMoO_4$ nanoparticles for high performance asymmetric supercapacitors. Electrochim. Acta, 2017, **238**, 337-348.

[S11] B. Senthilkumar, D. Meyrick, Y.-S. Lee and R. K. Selvan, Synthesis and improved electrochemical performances of nano β-$NiMoO_4$-$CoMoO_4 \cdot xH_2O$ composites for asymmetric supercapacitors. RSC Adv. 2013.

[S12] W.-L. Hong and L.-Y. Lin, Studying the substrate effects on energy storage abilities of flexible battery supercapacitor hybrids based on nickel cobalt oxide and nickel cobalt oxide@nickel molybdenum oxide. Electrochim. Acta, 2019, **308**, 83-90.

[S13] D. Wang, W. Zhu, Y. Yuan, G. Du, J. Zhu, X. Zhu and G. Pezzotti, Kelp-like structured $NiCo_2S_4$-C-MoS_2 composite electrodes for high performance supercapacitor. J. Alloys

Compd. 2018, **735**, 1505-1513.

[S14] X. Yu, B. Lu and Z. Xu, Super long-life supercapacitors based on the construction of nanohoneycomb-like strongly coupled $CoMoO_4$-3D graphene hybrid electrodes. Adv. mater., 2014, **26**, 1044-1051.

[S15] M.-C. Liu, L. Kang, L.-B. Kong, C. Lu, X.-J. Ma, X.-M. Li and Y.-C. Luo, Facile synthesis of $NiMoO_4 \cdot xH_2O$ nanorods as a positive electrode material for supercapacitors. RSC Adv, 2013, **3**, 6472-6478.